**RESEARCH ARTICLE**

# Application of $Co_9S_8@MoS_2$ core–shell/rGO nanocomposite as a novel electrocatalyst in preparation of sensor for the determination of metronidazole

Nasrin Lotfi[1] · Mir Reza Majidi[1] · Karim Asadpour-Zeynali[1,2]

## Abstract

This study is the first report on the application of $Co_9S_8@MoS_2$ core–shell nanoparticles decorated with reduced graphene oxide in the fabrication of an electrochemical sensor. This sensor exhibited great performance in the determination of metronidazole in blood plasma and tablet samples. These nanoparticles were synthesized via a facile and simple preparation method. First, Graphene oxide was synthesized via the Hummer method, and then $Co_9S_8@MoS_2$ core–shell nanoparticles were synthesized on the surface and edges of the reduced graphene oxide. In this way, the glassy carbon electrode was modified with $Co_9S_8@MoS_2$/Reduced graphene oxide nanoparticles. The nanocomposites were characterized by X-ray diffraction, transmission electron microscopy, scanning electron microscopy, energy dispersive X-ray, and Fourier transform infrared spectroscopy. The performance of the prepared sensor was studied by hydrodynamic amperometry and cyclic voltammetry techniques. A significant rise in the peak current and a considerable reduction in the overpotential of metronidazole were identified in the prepared sensor compared to the bare glassy carbon electrode. Under optimized conditions, two linear ranges of 0.5–35.0 μM and 35–180 μM and a limit of detection of 0.38 μM were obtained for metronidazole through the hydrodynamic amperometry technique using the proposed sensor. The $Co_9S_8@MoS_2$/Reduced graphene oxide sensor demonstrated good reproducibility, fast response, and a large specific area.

✉ Karim Asadpour-Zeynali
  asadpour@tabrizu.ac.ir; k.zeynali@gmail.com

1   Department of Analytical Chemistry, Faculty of Chemistry, University of Tabriz, Tabriz 51666-16471, Iran

2   Pharmaceutical Analysis Research Center, Faculty of Pharmacy, Tabriz University of Medical Sciences, Tabriz 51664, Iran

**Graphical Abstract**
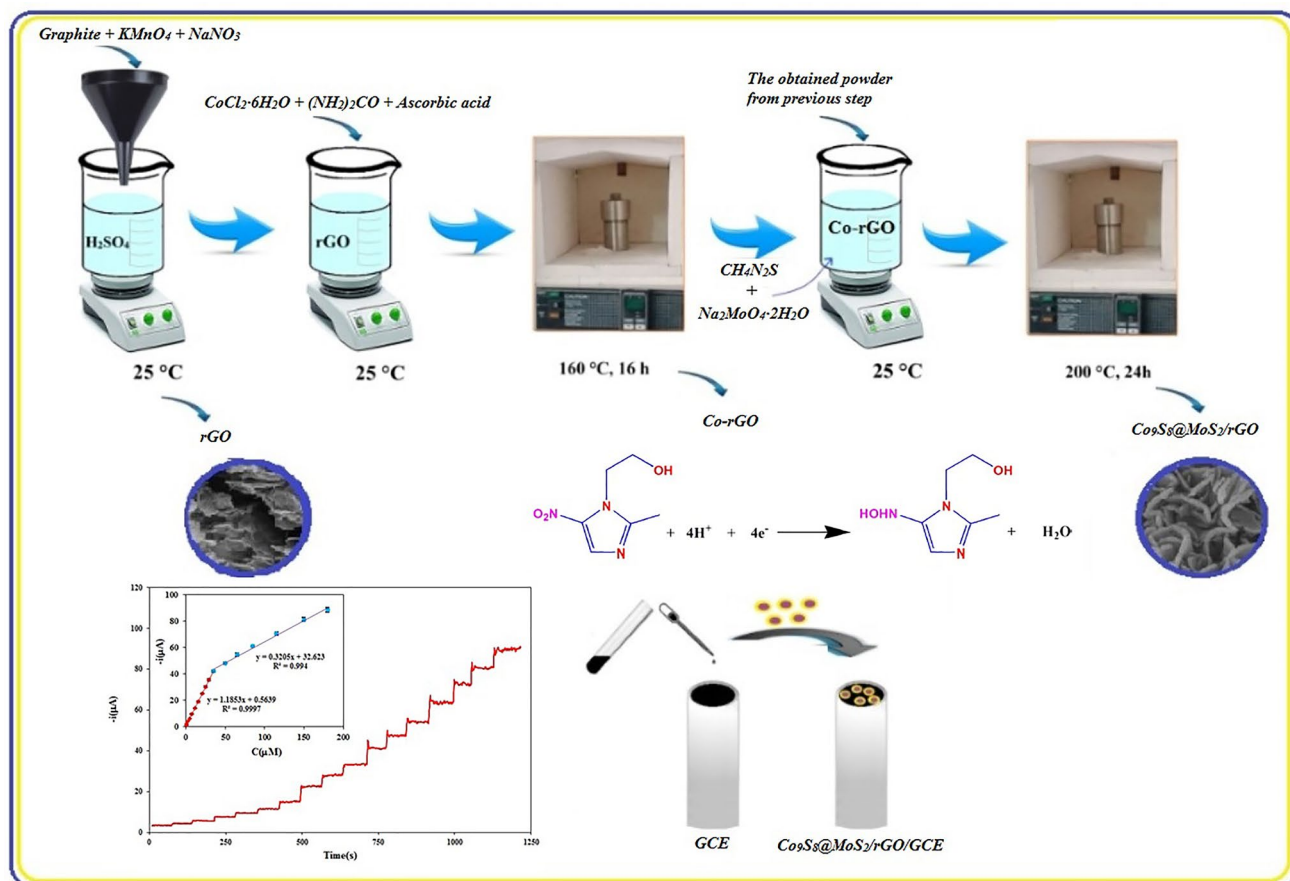


**Keywords** Nanosensor · $Co_9S_8@MoS_2$ · Core–shell · Electrocatalytic · Metronidazole

# 1 Introduction

Antibiotic medicines are one of the great successes of medical science that have increased the life expectancy of humans. Recently, the largest amount of drug production is related to antibiotics, which are used against protozoa, microalgae, parasites, viruses, bacteria, and fungi [1]. However, the use of some antibiotics has been restricted in some countries, including China, the United States, and Canada, due to their harmful effects [2, 3]. Metronidazole (MNZ), a nitroimidazole derivative, is an antiprotozoal medication and an antibiotic that can be either taken by mouth or intravenously; it can also be used in the form of a cream. MNZ, 2-methyl-5-nitroimidazole-1-ethanol, belongs to the nitroimidazole group of pharmaceuticals. MNZ is applied for the treatment of certain bacterial diseases, such as vaginal bacterial, liver, stomach, and skin infections, as well as joints, brain, and respiratory tract [4]. Additionally, MNZ is a veterinary drug that is used to treat bacterial infections in swine

and poultry [5]. It is also commonly used to prevent or treat echinococcosis caused by anaerobic bacteria and amoebic disease. Since this drug is not biodegradable, some undesirable effects like cardiogenic shock, pseudomembranous colitis, and peripheral neuritis can be diagnosed in clinical applications [6]. Overdose of the drug over a prolonged period can damage human health, wildlife, and the environment owing to its genotoxic, mutagenic, and carcinogenic side effects [7]. Headache, nausea, and loss of appetite are the other side effects of this medicine. In addition, a group of specialists believes that this drug should not be used in early pregnancy or lactation. Therefore, it is essential to extend a reliable, accurate, and sensitive procedure for the determination of MNZ. So far, it has been analyzed using various analytical methods, including chromatography [8, 9], spectrometric [10, 11], and electrochemical techniques [7, 12–18] Among the mentioned analytical techniques, electrochemical methods have been frequently used because of their fast response, low limit of detection, high sensitivity,

lack of need for time-consuming sample preparation and complicated separation methods, and inexpensive, and ease of use [7, 19–28]. However, electrochemical methods using bare/unmodified electrodes show poor practicality and sensitivity with lower electrochemical activity. Therefore, it is necessary to improve the performance of electrodes by modifying their surface [29, 30]. In this research field, a glassy carbon electrode (GCE) modified with graphene and a magnetic molecular polymer (mag-MIP) has been reported as an electrochemical sensor for the determination of MNZ [12]. In addition, an activated screen-printed carbon electrode [13], a GCE/biocompatible chitosan-pectin polyelectrolyte complex [14], a carbon paste electrode coated with graphene and sodium dodecyl sulfate (SDS) [15], a GCE coated with an eggshell-like hollow alumina sphere [7], a GCE modified with a $Fe_3O_4$/N/C/C@MWCNTs nanocomposite derivative from $H_2N$-Fe-MIL-88B metal–organic frameworks (MOFs) [16], a GCE modified with bismuth at a graphene via electrodeposition [17], a sensing platform based on green-synthesized magnetic $Fe_3O_4$ nanoparticles [18], a carbon nanofiber composite electrode decorated with composites of carbon nanofibers and orthorhombic iron-tungsten oxide (CNF/$Fe_2WO_6$) [27] and a GCE modified by binary mixed MOFs based on nickel and titanium [28] are only a part of the studies carried out for the electrochemical determination of MNZ.

Reduced graphene oxide (rGO), a carbon-based nanomaterial, has been recognized as an interesting material because it provides a larger surface area and accelerates the transfer of electrons between the analyte and the electrode, resulting in a faster and more sensitive current response [31]. Graphene oxide (GO) has a two-dimensional structure and exhibits excellent optical, thermal, electronic, and mechanical properties, with numerous applications in catalysis, sensors, electronics, energy conversion, storage, etc. With its unique structure and excellent properties, this carbon nanosheet provides an innovative way to prepare various multi-layer nanocomposites with better electrocatalytic activity [32], which have wide potential windows and suitable electrocatalytic activity for various redox reactions [33]. It is also worth mentioning the reduction of GO to rGO can create a single layer of graphene at a comparatively low cost. In recent years, sulfides of transition metals have been used as a fundamental category of functional materials. Among them, molybdenum disulfide is a layered material that has attracted considerable interest for application in the field of lithium-ion batteries owing to its improved cyclic stability and high theoretical capacity [34]. Moreover, $MoS_2$, which has many active unsaturated sulfur atoms, has been recognized as an efficient catalyst based on experimental and computational studies [35–37]. Although its moderate conductivity limits the electron transfer efficiency, electrode kinetics, and volumetric expansion upon cycling [34, 37, 38], chemists are still working to improve the catalytic properties of $MoS_2$ for various applications. One of the metallic transition metal sulfides with good thermal stability, comparatively high electrical conductivity, and theoretical capacity is cobalt sulfide ($Co_9S_8$), however, it shows poor electrochemical performance due to its slow mass transport kinetics [34–38]. It is worthwhile noting that cobalt sulfides exist in various phases, such as CoS, $CoS_2$, $Co_3S_4$, $Co_9S_8$. The combination of $MoS_2$ and $Co_9S_8$ provides many benefits, for instance, the synergistic effects can reduce the volume effect, improve the overall conductivity of the compounds, and improve the cycle performance and other electrochemical features of the sensor. The electrochemical efficiency of the nanocomposites can also be improved in a core–shell structure [34, 39–41]. Additionally, the combination of $MoS_2$ and $Co_9S_8$ in various structures such as nanocomposite or core–shell structures can increase the energy storage capacity of lithium batteries [34, 42–44]. This nanostructure has also been used for electrocatalytic hydrogen evolution activity [45]. The hydrothermal method/thermal solution, sonochemical method, and microwave radiation are among the synthesis methods of transition metal sulfides [46, 47]. In this work, the core–shell structure of $MoS_2$ and $Co_9S_8$ ($Co_9S_8$@$MoS_2$) decorated on rGO was formed to catalyze the electrochemical determination of MNZ in blood plasma and tablet samples. To the best of our knowledge, this nanostructure has been used for the first time to modify the surface of the electrode to determine the concentration of electroactive compounds in the field of measurement.

# 2 Experimental

## 2.1 Materials and methods

All reagents required for the synthesis of nanostructures and other analyses in the current research work are of analytical grade. Phosphate buffer solutions (PBS) were prepared by dissolving $K_2HPO_4$, $KH_2PO_4$, and $H_3PO_4$ in distilled water. All utilized chemicals in the manufacturing of $Co_9S_8$@$MoS_2$/rGO nanocomposite, $H_2SO_4$ (96%), $H_2O_2$ (30%), $KMnO_4$, $NaNO_3$, graphite powder, hydrazine hydrate, ammonia (25%), $CoCl_2 \cdot 6H_2O$, urea (($NH_2$)$_2$CO), ascorbic acid, thiourea ($CH_4N_2S$), sodium molybdate ($Na_2MoO_4 \cdot 2H_2O$), and ethanol ($C_2H_5OH$) were bought from Merck (Germany). Distilled water was procured from the Ghazi Company (Tabriz, Iran). Human blood serum samples were obtained from the Iranian Blood Transfusion Research Centre (Tabriz, Iran).

A Potentiostat Autolab instrument PGSTAT 30 ECO Chemie (The Netherlands) was used to collect electrochemical data and sensing analyses including, CVs, DPVs, and amperometric responses. Furthermore, the modified GCE was used

alongside a conventional three-electrode system, including a platinum electrode as the auxiliary electrode, a saturated calomel electrode (SCE: Hg/Hg₂Cl₂/Saturated KCl solution) as the reference electrode, and an electrochemical cell. All electrodes used in this study were purchased from the Azar Electrode Company (Urmia, Iran). Electrochemical impedance spectroscopy was performed at an open circuit using Autolab potentiostat (model PGSTAT30) and impedance software ZView (II) and Nova 2.1. The morphological characterizations of the prepared $Co_9S_8@MoS_2/rGO$ core–shell nanocomposites were studied using field emission scanning electron microscopy (FESEM). The elemental composition was studied by energy dispersive X-ray spectroscopy (EDX) in a TESCAN MIRA3 and the core–shell structure of the synthesized nanostructure was investigated by an LEO 906 transmission electron microscope (TEM, Zeiss, Germany). Moreover, X-ray diffraction patterns were recorded using a Bruker AXS (D8 Advance) X-ray powder diffractometer (Cu Kα radiation source, $\lambda = 0.154056$ nm) in the 2θ range of 10–70° at 35 mA and 40 kV at room temperature (Germany). The FTIR spectrum was obtained using a Shimadzu 8400 series (Japan) Fourier transform infrared spectrometer. A pH meter Metrohm 827 was used to adjust the pH of the aqueous solutions (Switzerland Metrohm Company).

## 2.2 Synthesis of the reduced graphene oxide (RGO)

Graphite powder was used to synthesize GO by Hamer's method. Briefly, 1 g of graphite powder was added to 30 mL of $H_2SO_4$ in an ice bath and stirred. Then 1 g of the weighed $NaNO_3$ powder was poured into the above suspension and stirred for an hour. Afterward, 3.6 g of $KMnO_4$ was gradually added over 2 h. Then the temperature was increased to 35 °C and the mixture was stirred for 2 h. In the next step, 46 mL of double-distilled water was poured into the above mixture and stirred at 90 °C for 30 min. The reaction was completed by adding 12 mL of $H_2O_2$ (30%) and 120 mL of deionized water. Finally, the precipitated material was collected, washed, and dried in an oven at 60 °C.

To prepare rGO, the required amount of GO was dispersed in double distilled water for 2 h, and 20 mL of a 50:50 solution of hydrazine hydrate and 25% ammonia was poured into the above reaction vessel. Finally, the solution was refluxed at 85 °C for 1 h, collected, washed, and then dried in an oven at 60 °C [48].

## 2.3 Chemical synthesis of the $Co_9S_8@MoS_2/rGO$ core–shell nanocomposite

The $Co_9S_8@MoS_2/rGO$ core–shell nanoparticles were synthesized as described in the reference [34]. Accordingly, Co-rGO was synthesized in the first step as follows. First,

28 mg of rGO was dispersed in 70 mL of deionized water for 5 h to obtain a homogeneous solution. Then, 0.07 g of $CoCl_2.6H_2O$, 0.042 g of urea ($(NH_2)_2CO$), and 0.056 g of ascorbic acid were added to the above homogeneous solution with rapid stirring. The mixture was transferred to a Teflon-lined 100 mL autoclave and held at 160 °C for 16 h. The synthesize the $Co_9S_8@MoS_2/rGO$ core–shell nanocomposite, the resulting precipitate was collected by centrifugation and eluted three times with a 50:50 solution of ethanol and water and then dried at 60 °C. In the next step, 0.025 g of $Na_2MoO_4\cdot2H_2O$, and 0.08 g of thiourea were completely dissolved in 30 mL of solvent mixtures ($H_2O:C_2H_5OH = 1:1$). Afterward, 0.05 g of the precursor was transferred to the solution under vigorous magnetic stirring. Subsequently, the mixture was transferred to a 50 mL Teflon autoclave and finally, it was placed in the oven at 200 °C for 24 h, which led to the formation of a dark deposit. Upon centrifugation, $Co_9S_8@MoS_2/rGO$ was obtained as the black product.

## 2.4 Synthesis of $Co_9S_8/rGO$

Initially, 0.05 g of thiourea was dissolved in 30 mL of a mixed solvent ($H_2O:C_2H_5OH = 1:1$, in volume). Then, 0.05 g of the Co-GO precursor was added to the above mixture, stirred vigorously at 45 °C for 2 h, transferred into a 50 mL Teflon-lined autoclave, and kept at 200 °C for 24 h. The obtained black precipitate was washed with deionized water and ethanol 5 times and dried at 60 °C for 8 h.

## 2.5 Preparation of the $Co_9S_8@MoS_2/rGO/GCE$ sensor

To prepare the sensor, the surface of GCE was polished with alumina powder and ultrasonically rinsed in ethanol and water (50:50) for 15 min to eliminate impurities. Then a suspension of 0.005 g/mL of the synthesized nanostructure was prepared in distilled water. Next, an optimal value of 4 μL drops of the above suspension was dropped onto the GCE surface and dried at 25 °C.

## 2.6 Preparation of real samples

Five MNZ tablets (250 mg per tablet) purchased from a local pharmacy were carefully weighed and ground. The average weight of one tablet (0.4125 g) was transferred to a 100 mL flask containing distilled water and sonicated for 20 min. The centrifugation of a portion of the resulting solutions was followed by the supernatant solution analysis. MNZ was determined using the human blood plasma sample prepared by the Blood Transfusion Organization. One mL of the MNZ standard solution was added to a 15 mL falcon containing 1 mL of the blood plasma. After stirring the mixture, 1 mL of acetonitrile was added to precipitate the plasma proteins and then centrifuged at 6000 rpm for 15 min. Afterward,

0.5 mL of the clear supernatant solution was transferred to a 10 mL flask and made up with 0.1 M of PBS (pH = 7).

# 3 Results and discussion

## 3.1 Morphological characterizations

The crystal phase, structure, and morphology of the prepared sensor surface were characterized by SEM, EDX, and TEM. The SEM images of rGO (A) and $Co_9S_8$@$MoS_2$/rGO (B) show the $Co_9S_8$@$MoS_2$ core–shell nanoparticles on the surface and edges of the rGO plates (Fig. 1). Moreover, the quantitative EDX analysis of rGO and $Co_9S_8$@$MoS_2$/rGO nanoparticles confirmed the presence of the mentioned elements in the modifier (Fig. 1a, b). Figure 1C shows the TEM image of the $Co_9S_8$@$MoS_2$ core–shell nanostructure. A clear lattice fringe around the opaque core is a characteristic of the core–shell structure of the synthesized nanostructure. Moreover, the XRD patterns of $Co_9S_8$@$MoS_2$/rGO and rGO (Fig. 2A and B) are consistent with the references used to synthesize this nanocomposite [34]. $Co_9S_8$ nanoparticles serve as a core, while $MoS_2$ nanoparticles grow on the $Co_9S_8$ surface to form a core–shell structure. The XRD and SEM results support this conclusion. A distinct peak located at 14.1° corresponds to the (002) crystalline plane of $MoS_2$. The peaks of 15.2, 25.5, 29.8, 31.1, 47.5, and 52.0° match well with the (111), (220), (311), (222), (511), and (440) crystalline planes of cubic-phase $Co_9S_8$. In addition, the broad peak centered at 26.0° can be assigned to the (002) crystalline plane of the rGO which is rich in graphene. Combined with the XRD and SEM results, it can be concluded that the $Co_9S_8$ nanoparticles serve as a core and the $MoS_2$ nanosheets grow on the surface of the $Co_9S_8$ nanoparticles to form the core–shell structure [42].

X-ray diffraction is a suitable method for determining the average size of nanocrystallites in bulk materials. X-Ray diffraction is sensitive to the crystallite size inside the particles. From the Scherrer equation, the average size of nanoparticles, L, is as follows:

$$L = \frac{K\lambda}{\beta\cos\theta}$$

where λ is the X-ray wavelength (0/154056 nm), β is the peak width of the diffraction peak profile at half maximum height resulting from the small crystallite size, in radians, and K is a constant related to the crystallite shape and usually assumed to be 0.9 [49]. By calculating L for all peaks and computing the average, an approximate nanoparticle size of 62 nm was obtained.

The functional groups of the synthesized compounds were identified using the FT-IR technique. The FT-IR spectrum of the $Co_9S_8$@$MoS_2$/rGO nanostructure in the range of 400–4000 $cm^{-1}$ is shown in Fig. 2C. The peaks at 1631 and 1408 $cm^{-1}$ in the spectrum belong to the C–O stretching vibration of the epoxide [50], and the stretching vibration of tertiary C–OH groups, the peak at 1070 $cm^{-1}$ belongs to carboxyl and carbonyl groups and the C=O stretching vibration [51]. A sharp vibrational peak in the region of 3403 $cm^{-1}$ can be assigned to the stretching vibration of the O–H group bonding. In addition, two absorption bands at 3297 $cm^{-1}$ and 1569 $cm^{-1}$ can be assigned to the stretching and bending vibrations of water adsorbed on the surface of the samples, respectively [52]. A peak at 865 $cm^{-1}$ is attributed to the Co-S bonding and its stretching vibration. The peak of the bending vibration observed at 1144 $cm^{-1}$ belongs to a sulfonated group of $Co_9S_8$ and is merged with the $CO_2$ absorption band [53]. The peaks associated with the bond (Mo–S), δ(C=S) and δ(C–S) are at 951 $cm^{-1}$, 465 $cm^{-1}$, and 1128 $cm^{-1}$, respectively.

## 3.2 The electrical conductivity of the sensor

Electrochemical impedance spectroscopy (EIS) is a powerful method for testing the electrical conductivity properties of a modified electrode. The electrical conductivity of the bare GCE, and GCE modified with rGo, $Co_9S_8$/rGO, and $Co_9S_8$@$MoS_2$/rGO was investigated using the EIS technique and compared with the bare GCE. ZView impedance software (II) and Nova 2.1 were used to fit the data to the Nyquist spectra of the impedance data. The Nyquist curve of the EIS (Nyquist plots corresponding to the real part Z′ versus the imaginary part -Z″ of the complex impedance Z) contains a linear part and a semicircular part. A decrease in the radius of the semicircle in the Nyquist curve indicates high electrical conductivity and low resistance of electron transfer at the electrode surface. Figure 3A shows the Nyquist spectrum of the $Co_9S_8$@$MoS_2$/rGO/GCE (d), $Co_9S_8$/rGO/GCE (c), rGO/GCE (b) sensors, and the bare GCE (a) in 1.0 mM $[Fe(CN)_6]^{3-/4-}$ containing 0.1 M KCl. The $Co_9S_8$@$MoS_2$/rGO/GCE sensor has a much smaller semicircle, the lowest resistance, and faster charge transfer than $Co_9S_8$/rGO/GCE, rGO/GCE sensors, and the bare GCE. Based on Fig. 3B, the reduction of the redox potential and the current improvement confirm the content above.
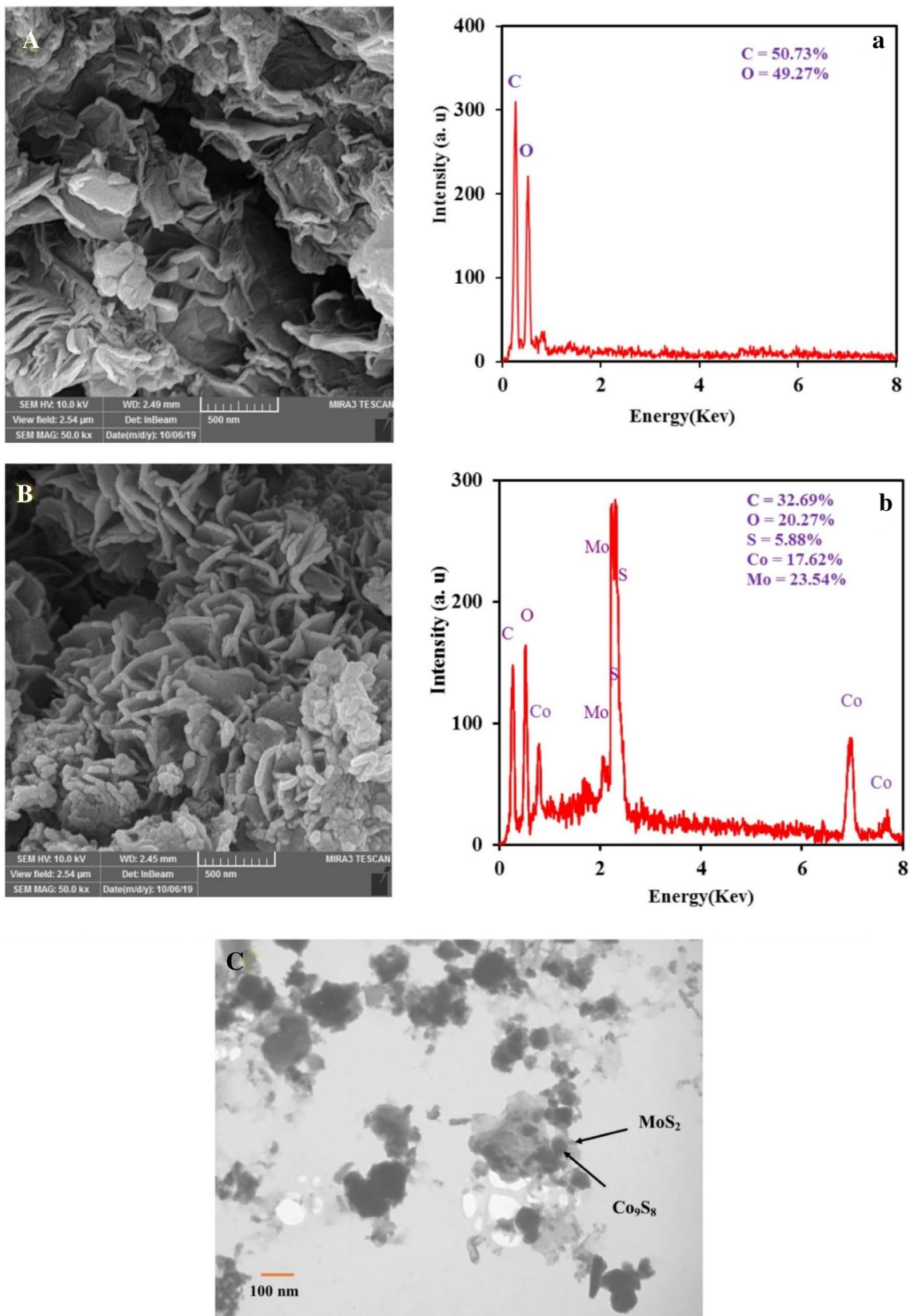
**Fig. 1** SEM images of rGO (**A**), $Co_9S_8@MoS_2/rGO$ (**B**), EDX patterns rGO (**a**), $Co_9S_8@MoS_2/rGO$ (**b**)

**Fig. 2** **A** XRD patterns of $Co_9S_8@MoS_2/rGO$, **B** rGO, **C** FT-IR spectrum of $Co_9S_8@MoS_2/rGO$
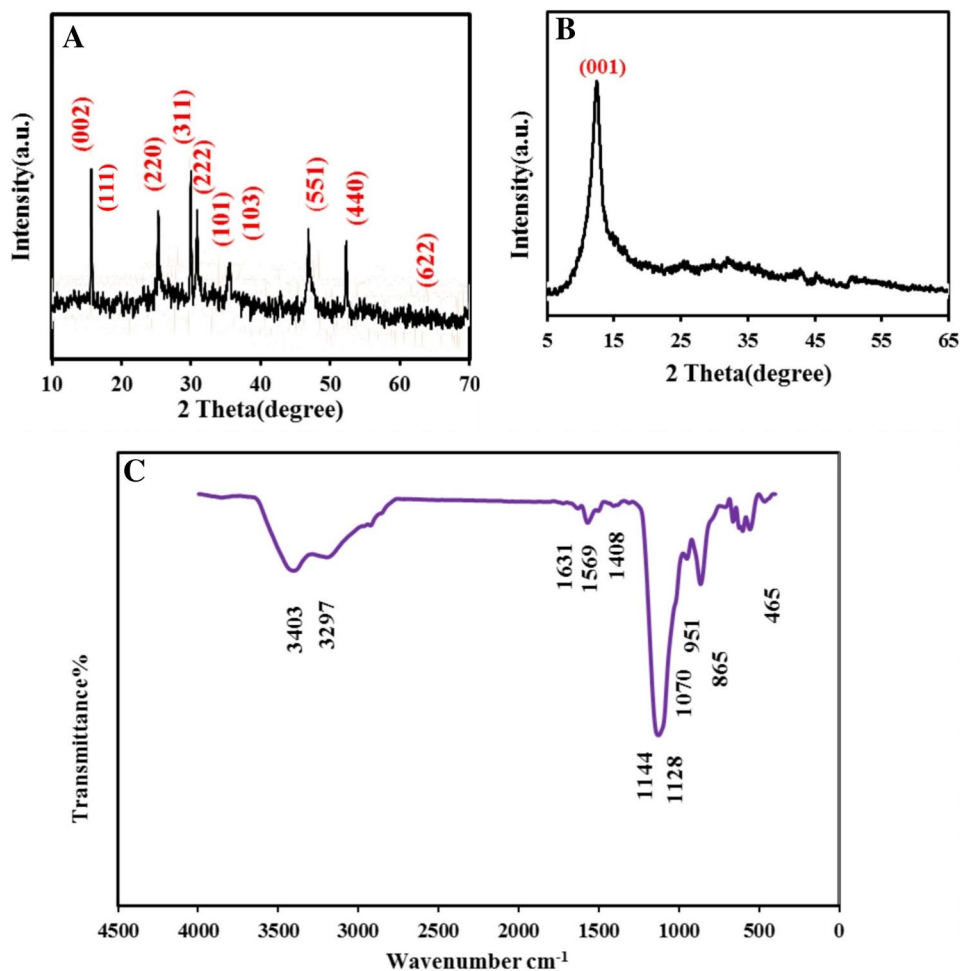


**Fig. 3** **A** EIS analysis of (a) the bare GCE, (b) rGO/GCE, (c) $Co_9S_8$/rGO/GCE, and (d) $Co_9S_8@MoS_2$/rGO/GCE in 0.1 M KCl solution containing 1.0 mM $[Fe(CN)_6]^{3-/4-}$. Inset (c): Equivalent circuit applied to fit impedance measurements; **B** Corresponding CVs (a) Bare GCE, (b) rGO/GCE, (c) $Co_9S_8$/rGO/GCE, (d) $Co_9S_8@MoS_2$/rGO/GCE
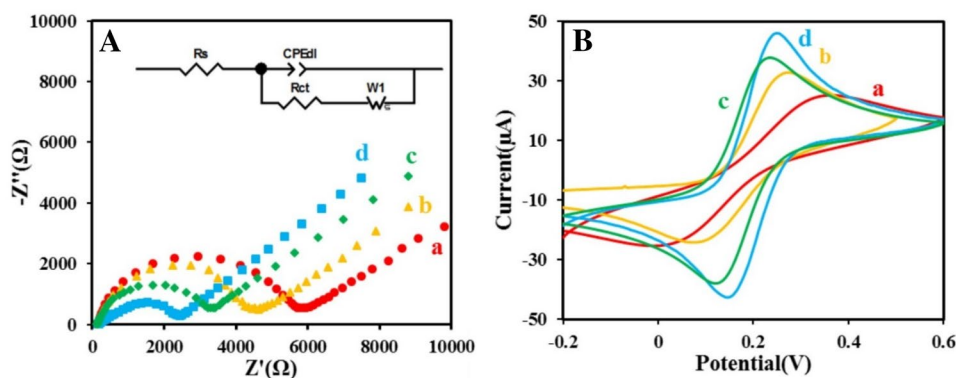


## 3.3 Electrochemical behavior of MNZ on the surface of the bare GCE, rGO/GCE, $Co_9S_8$/rGO/GCE, and $Co_9S_8@MoS_2$/rGO/GCE sensor

The electrochemical behavior of MNZ on the surface of the bare GCE, rGO/GCE, $Co_9S_8$/rGO/GCE, and $Co_9S_8@MoS_2$/rGO/GCE sensor was compared by cyclic voltammetry (CV) in 0.1 M of the PBS solution (pH = 7) containing $1 \times 10^{-4}$ M of MNZ. Figure 4 compares the CVs of the modified electrodes with those of GCE in $1.0 \times 10^{-4}$ M of MNZ. Accordingly, improving the modifier and increasing its surface-to-volume ratio increases the cathodic peak current, and shifts the cathodic peak potential to a lower potential, indicating an enhancement
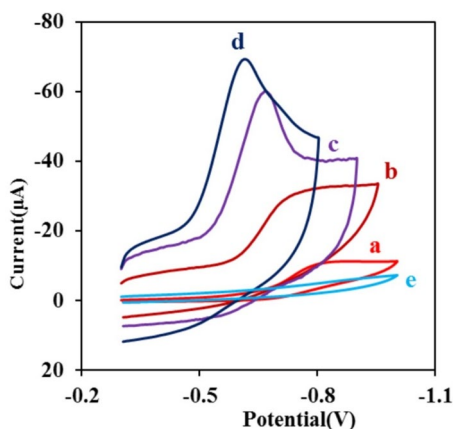
**Fig. 4** (A) CVs of $1 \times 10^{-4}$ M of MNZ at (a) the bare GCE, (b) the rGO/GCE, (c) $Co_9S_8$/rGO/GCE, (d) $Co_9S_8$@$MoS_2$/rGO/GCE, and Curve of (e) is the CV of the $Co_9S_8$@$MoS_2$/rGO/GCE nanosensor without MNZ in 0.1 M of PBS (pH = 7), scan rate: 0.05 Vs.$^{-1}$

in electron transfer due to the larger surface area of the $Co_9S_8$@$MoS_2$/rGO/GCE sensor. It is worth noting that the cathodic peaks seen in Fig. 4 are related to the electrocatalytic reduction of MNZ.

### 3.4 Effective surface area of the sensor

The active surface area of the electrode was increased by modifying the GCE surface with semiconductor nanocomposites $Co_9S_8$@$MoS_2$/rGO. Increasing the active surface of the electrode makes it easy for electrons to reach the electrode and exchange electrons in the reactions. The active surface area of the modified electrode was calculated using the cyclic

voltammetry technique in the solution of 0.1 M supporting the electrolyte of KCl containing 1.0 mM of $[Fe(CN)_6]^{3-/4-}$. The area of the active surface can be calculated according to the CVs shown in Fig. 5A and the following equation (Randles–Sevcik):

$$I_p = (2.69 \times 10^5)n^{3/2}AD^{1/2}v^{1/2}C_0$$

where $I_p$ is the peak current, $C_0$ refers to the concentration of $[Fe(CN)_6]^{3-/4-}$, n is the number of electrons exchanged, A is the area of the active surface of the modified electrode, v is scan rate, and D is the diffusion coefficient of $[Fe(CN)_6]^{3-/4-}$. $I_p$ should have a linear relationship with the $v^{1/2}$. By recording CVs at different scan rates and drawing the Ipa-$v^{1/2}$ diagram (D = $7.6 \times 10^{-6}$ cm$^2$ s$^{-1}$ and n = 1), the surface area of the $Co_9S_8$@$MoS_2$/rGO/GCE sensor was calculated from the slope of the diagram in Fig. 5B (slope = 0.0000707 A/Vs$^{-1}$). Eventually, A was found to be 0.0945 cm$^2$, which is a three-fold increase over the bare GCE (0.0314 cm$^2$).

### 3.5 Scan rate and kinetic investigation

To study the effect of scan rate and reaction kinetics as well as the nature of the electrode process, the cyclic voltammograms of the sensor were recorded at the scan rates of 5–210 mVs$^{-1}$ in 0.1 M of PBS (pH = 7) solution containing $1 \times 10^{-4}$ M of MNZ. The peak potential showed a slight shift toward the cathodic direction (Fig. 6A), revealing that the reduction of MNZ at the $Co_9S_8$@$MoS_2$/rGO/GCE sensor is an irreversible process. Figure 6B shows a linear relationship between the cathodic peak current ($I_{pc}$) and the square root of the scan rate ($V^{1/2}$), hence the reduction of MNZ is a diffusion-controlled process.

**Fig. 5** **A** CVs of the modified GCE with $Co_9S_8$@$MoS_2$/rGO in 0.1 M KCl solution containing 1.0 mM $[Fe(CN)_6]^{3-/4-}$ at scan rates (inner to outer) of 10, 25, 45, and 70 mVs$^{-1}$, **B** peak current diagram against the square root of the scan rate
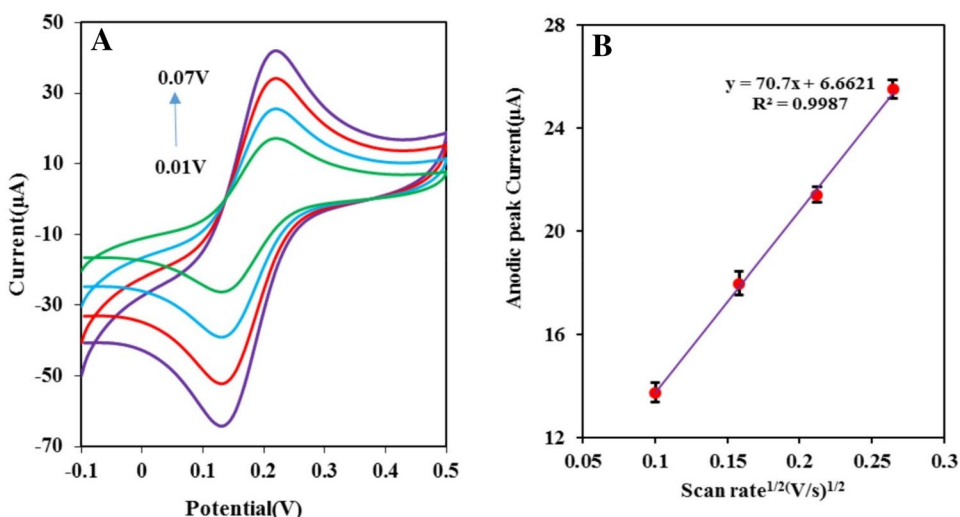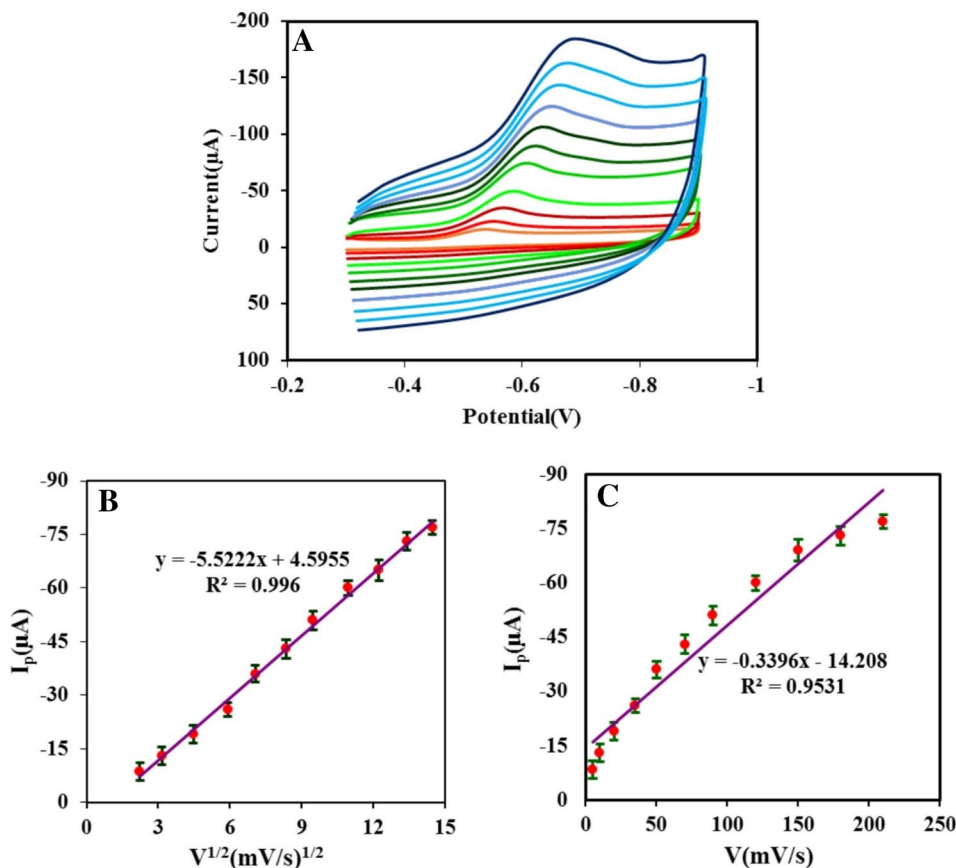
**Fig. 6** **A** CVs of $1 \times 10^{-4}$ M MNZ in 0.1 M of PBS (pH = 7) on the $Co_9S_8@MoS_2/rGO/GCE$ sensor at different scan rates from 5 to 210 mVs$^{-1}$. **B** Linear relationship of cathodic peak current ($I_{pc}$) of MNZ Vs scan rate. **C** Relationship of cathodic peak current ($I_{pc}$) of MNZ Vs square root of scan rate

The electrochemical behavior of MNZ on the surface of $Co_9S_8@MoS_2/rGO/GCE$ was studied by the chronoamperometric method. To this aim, the chronoamperograms were recorded for the modified electrode with a known surface area in the static solution of MNZ with a concentration range of 0.1–0.7 mM in 0.1 M of PBS (pH = 7), and in a potential of − 0.7 V. The recorded chronoamperograms are shown in Fig. 7A. In Fig. 7B, was plotted I versus $t^{-1/2}$. Finally, the slope of the graphs in Fig. 7B was plotted versus the MNZ concentration (Fig. 7C). Diffusion coefficient of MNZ can be obtained according to the recorded charts and the Cottrell equation:

$$I = nFAD^{1/2}C\pi^{-1/2}t^{-1/2}$$

where I is the current intensity in amperes, n is the total number of MNZ electrons exchanged (n = 4), F is the Faraday number (96,489 C), C is the concentration of the electroactive compound in mol/cm$^3$, t is the time in seconds, D is the diffusion coefficient, and A is the surface area of the modified electrode (0.0945 cm$^2$). The diffusion coefficient of MNZ was $4.98 \times 10^{-6}$ cm$^2$ s$^{-1}$, which is comparable to the values obtained in previous articles [7, 23].

## 3.6 The effect of pH

The pH of biological samples is very important, and this parameter of the electrolyte plays an essential role in redox reactions. Therefore, the effect of the electrolyte pH on the reduction peak of MNZ was studied in the range of 3–10 with the prepared sensor for $1 \times 10^{-4}$ MNZ at a scan rate of 50 mVs$^{-1}$. Figure 8 shows the resulting CVs of MNZ reduction in the solutions with different pH values. As shown in Fig. 8A, the cathodic peak potential shifted to a negative potential with increasing pH, which is due to the participation of proton(s) in the reduction reaction of MNZ. According to the slope of the graph in Fig. 8B(0.0554 V/pH), which shows the Nernst behavior of the sensor, the number of exchanged electrons is equal to that of protons participating

**Fig. 7** **A** Chronoamperograms in the presence 0.1–0.7 mM of HZ at potential $-$ 0.5 V vs. SCE, **B** Plots of $I - t^{-1/2}$ for various MNZ concentrations and **C** slope values of $I - t^{-1/2}$ plots versus HZ concentrations
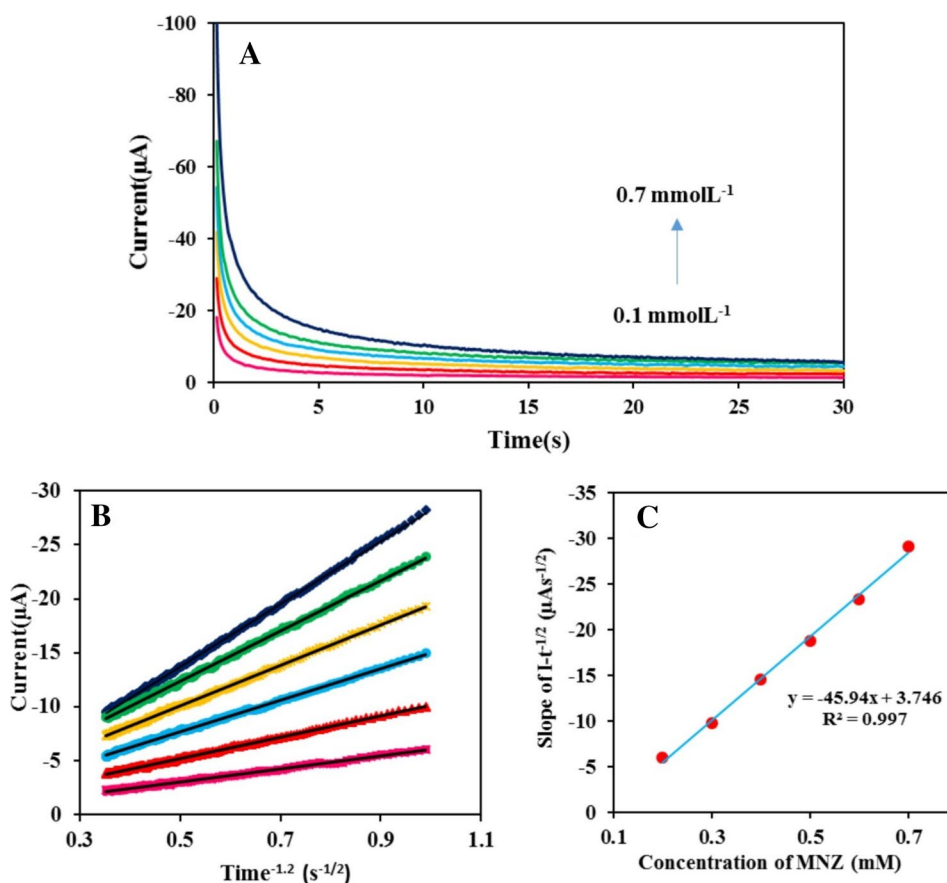


in the reduction reaction of MNZ and 1$-$ (2hydroxyethyl) $-$2 methyl 5 nitroimidazole to 1$-$ (2hydroxyethyl) $-$2 methyl hydroxyamide imidazole. Since MNZ has two pka, it is likely to be involved in acidic and basic reactions in acidic and basic solutions, and the reduction reaction is not easily done (Scheme 1).

Due to the importance of pH measurement in the biological environment and referring to the diagram of MNZ cathodic peak currents ($I_{pc}$) versus different pH values, an optimum pH value of 7 was chosen in this work (Fig. 8C).

### 3.7 The amperometric detection of MNZ on the Co$_9$S$_8$@MoS$_2$/rGO/GCE sensor

In this study, the hydrodynamic amperometry technique was used at a constant electrode potential to study the performance of the Co$_9$S$_8$@MoS$_2$/rGO/GCE sensor as an amperometric sensor in the determination of MNZ. Figure 9A shows current–time responses obtained by the Co$_9$S$_8$@MoS$_2$/rGO/GCE sensor at the applied potential of

-0.8 V for the successive additions of MNZ to a 10 mL supporting electrolyte which was stirred with different increments. The linear responses of the Co$_9$S$_8$@MoS$_2$/rGO/GCE sensor to MNZ were in the concentration ranges of $5.00 \times 10^{-7}$–$3.50 \times 10^{-5}$ M and $3.50 \times 10^{-5}$–$1.80 \times 10^{-4}$ M (Fig. 9B). Moreover, the calculated limit of detection (LOD) was $0.38 \times 10^{-6}$ M based on the signal-to-noise ratio (S/N) of 3 in the initial part of the calibration curve. At the higher concentrations for the analyte, the active sites of Co$_9$S$_8$@MoS$_2$/rGO on the surface of the modified electrode maybe not be enough to reduce MNZ, and two linear ranges were observed.

### 3.8 The application of the Co$_9$S$_8$@MoS$_2$/rGO/GCE sensor in real samples

The capability of the fabricated sensor was examined by determining the concentration of MNZ in real samples of MNZ tablets and human serum samples with MNZ spiked by hydrodynamic amperometry. When MNZ was

**Fig. 8** **A** CVs of $1 \times 10^{-4}$ M of MNZ on the $Co_9S_8$@$MoS_2$/rGO/GCE sensor in 0.1 M of PBS at different pH values (3–10): **B** Linear relationship of $E_{pa}$ Vs pH. **C** Effect of pH on the reduction peak currents
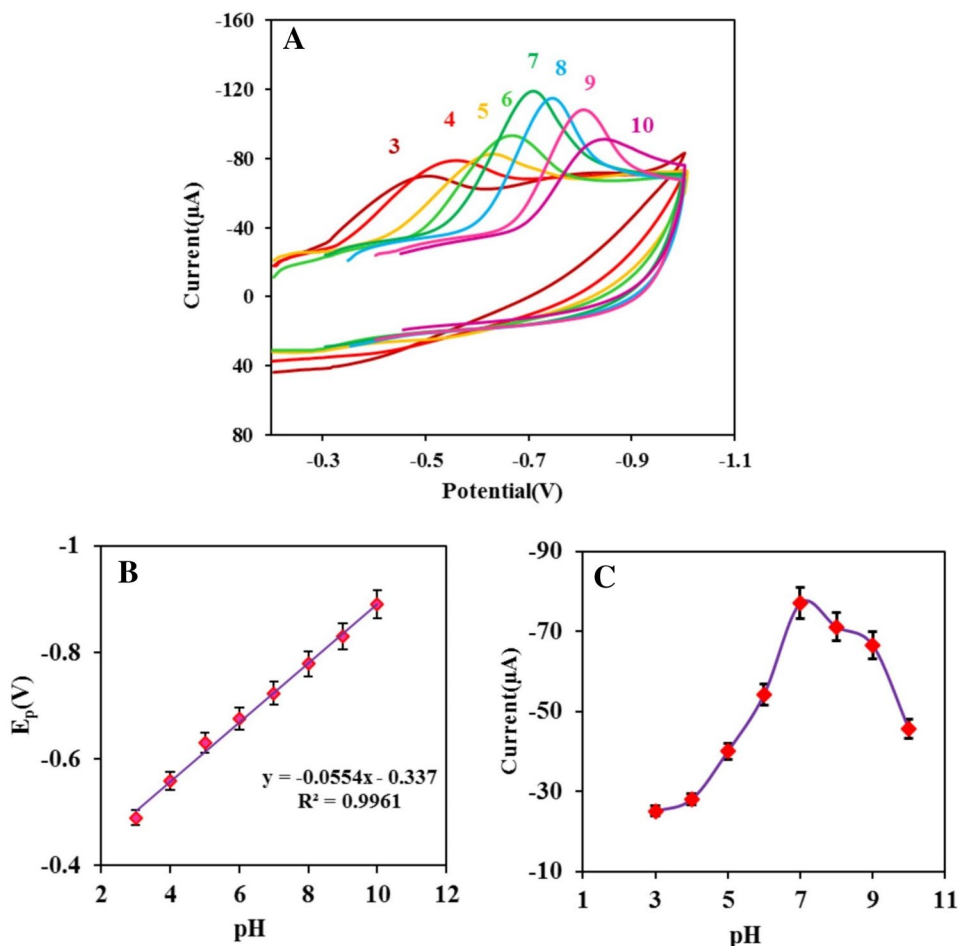


**Scheme 1** Electrochemical Reduction Mechanism of MTZ [13, 54]
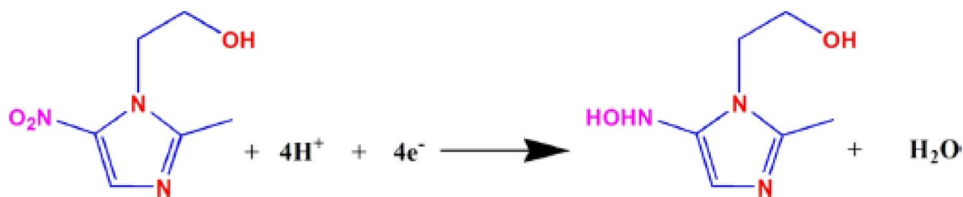


determined in the tablet sample, the MNZ concentration in the electrochemical cell was estimated to be 1.5 μM and the MNZ-spiked in the human serum sample was estimated to be 2.3 μM, as indicated by the information on the drug package and the calculations. Therefore, the same signal with the proposed sensor was observed with the least error. These measurements were repeated thrice, and the obtained relative standard deviation (RSD) values (2.6% and 3.3%, respectively) indicated the satisfactory repeatability of the electrode. (Table 1). Table 2 compares the results of the

efficiency of the sensor prepared in this research study with the methods reported in previous articles.

## 3.9 Interference studies

Electrochemical sensors for the detection of MNZ are interfered with by compounds with similar chemical structures. Therefore, possible interference must be carefully investigated to verify the sensitivity of the proposed sensor. Under

**Fig. 9 A** Amperometric response of $Co_9S_8@MoS_2/rGO/GCE$ sensor for the increasing concentrations of MNZ in 0.1 M of PBS (pH = 7). Scan rate: 0.05 $Vs^{-1}$ and pulse amplitude: 50 mV. **B** Calibration curve for the different concentrations of MNZ
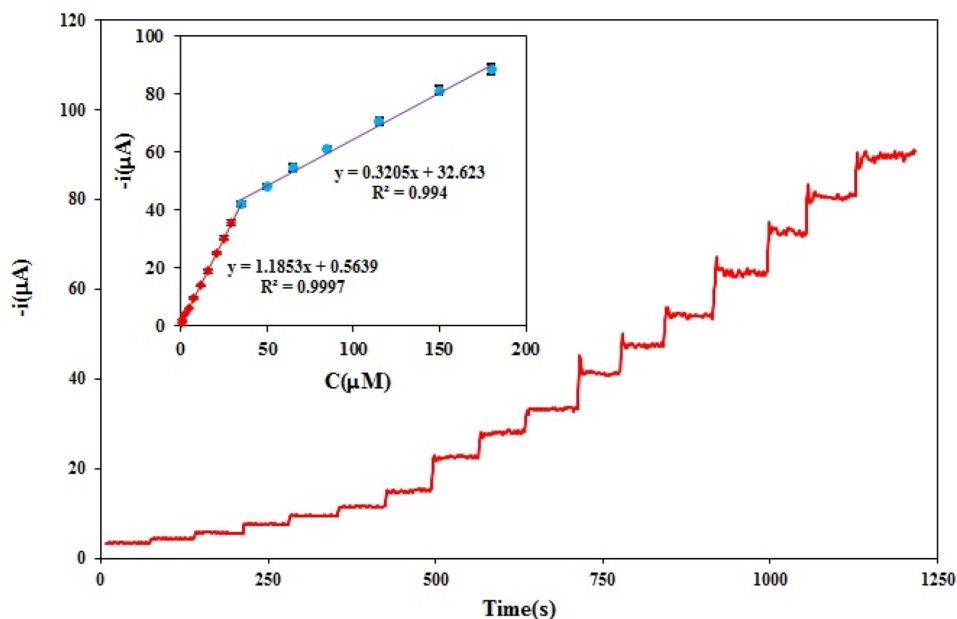


**Table 1** Results of recoveries of MNZ in drug samples and Human serum

| Samples | Initial MNZ (μM) | Added MNZ (μM) | Found MNZ (μM) | Number of experiments | RSD | Recovery |
|---|---|---|---|---|---|---|
| Tablet | 1.5 | 0 | 1.48 | 3 | 2.6% | – |
| | 1.5 | 5 | 6.42 | 3 | 1.3% | 98.8 |
| Human serum | 2.3 | 0 | 2.32 | 3 | 3.3% | – |
| | 2.3 | 3 | 5.38 | 3 | 1.47% | 101.5 |

**Table 2** Comparison of the performance of the proposed method with previously reported methods

| Year | Electrode-modifier | Measurement method | Linear range (μm) | LOD | References |
|---|---|---|---|---|---|
| 2019 | GCE-CuCo$_2$O$_4$/N-CNTs/MIP | Differential pulse voltammetry | 0.005–0.1, 0.1–100 | 0.48 nM | [6] |
| 2019 | GCE-ZIF-67C@rGO-0.06 | Differential pulse voltammetry | 0.5–1000 | 0.05 μM | [10] |
| 2019 | GCE-CS-PC BPE | Differential pulse voltammetry | 0.01–465 | 0.009 μM | [14] |
| 2018 | CPE-SDS | differential pulse stripping voltammetry | 0.08–200 | 8.5 nM | [15] |
| 2019 | GCE-Fe$_3$O$_4$/N/C@MWCNTs | Differential pulse voltammetry | 1–10, 10–725 | 0.19 μM | [16] |
| 2022 | Fe$_2$O$_3$@GO/GCE | Hydrodynamic amperometry | 1–1680 | 55 nM | [24] |
| 2020 | ZnCo-MOF/GCE | linear sweep voltammetry | 0.05–100 | 17 nM | [23] |
| 2021 | RGO-oct-Mn$_3$O$_4$/GCE | Differential pulse voltammetry | 0.1–9.5 | 0.037 μM | [24] |
| 2023 | GCE/CNF/Fe$_2$WO$_6$ | Differential pulse voltammetry | 0.01–1792 | 0.013 μM | [27] |
| 2023 | GCE-binary mixed Mof of Ni and Ti | Differential pulse voltammetry | 0.1–200 | 0.03 μM | [28] |
| 2020 | NiFe-LDH/sulfur-doped carbon nitride arrays | Hydrodynamic amperometry | 0.008–110.77 | 1.6 nm | [55] |
| 2023 | GCE-O$_9$S$_8$@MoS$_2$/rGO | Hydrodynamic amperometry | 0.5–35.00, 35–180 | 0.38 μM | This work |

optimal conditions, biological samples such as uric acid (UA), oxalic acid (OA), malic acid (MA), glucose, ascorbic acid (AA), and acetaminophen (AC), as well as metal ion samples such as $Cl^-$, $NO^{3-}$, $Cu^{2+}$, $Fe^{2+}$, $Fe^{3+}$, $Na^+$, and $K^+$ were selected for interference studies (Fig. 10). The results of this analysis are shown in Table 3. The presence of the aforementioned biological samples and metal ions results in a slight change in the current value. In the presence of

**Fig. 10** Amperometric responses of different concentrations of interfering compounds on $Co_9S_8@MoS_2/rGO/$ GCE sensor in 0.1 M of PBS (pH = 7) with 50 μM of MNZ
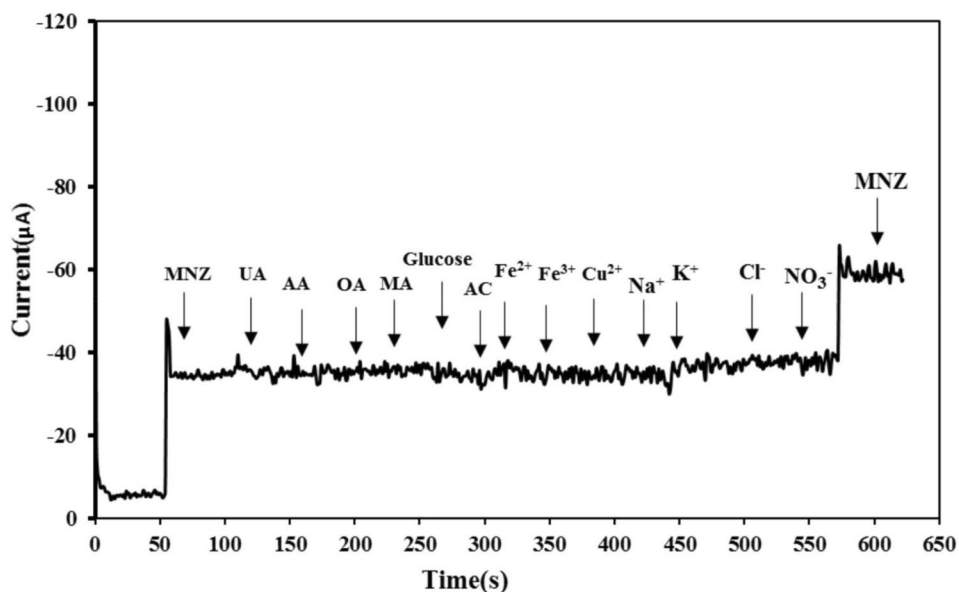


biological samples 10 times higher than the MNZ concentration (50 μM), the electrochemical signal related to MNZ shows a slight change of about 2.3%. In the presence of six-fold metal ions, this signal change was 2.8%. Therefore, the proposed sensor is suitable for the determination of MNZ.

### 3.10 The stability and reproducibility of the $Co_9S_8@$ $MoS_2/rGO/GCE$ sensor

Cyclic voltammetry tests were performed to examine and determine the stability, repeatability, and reproducibility in $1 \times 10^{-4}$ M of MNZ (0.1 M of PBS pH = 7), in the potential range of − 0.3 to − 0.9 V, and a scan rate of 50 mVs$^{-1}$. Besides, 100 cyclic voltammetry scans were applied in the stability test. The peak current and peak potential of the first scan and the 100th scan were compared with each other and

**Table 3** Effects of interfering species on the electrochemical determination of MNZ at $Co_9S_8@MoS_2/rGO/GCE$

| Interfering species | MNZ concentration | Interfering concentration | RSD |
|---|---|---|---|
| Cl$^-$, NO$_3{}^{3-}$, Cu$^{2+}$, Fe$^{2+}$, Fe$^{3+}$, Na$^+$, and K$^+$ | 50 μM | 300 μM | 2.8% |
| Oxalic acid, ascorbic acid, uric acid, malic acid, glucose, acetaminophen | 50 μM | 500 μM | 2.3% |

the differences in both cases were less than 2.1% (Fig. 11A). To investigate the effect of aging on the electrode, an electrode was prepared in optimal conditions and examined on different days from 1 to 7 days. It was observed that the peak current decreased by 4.8% after 7 days (Fig. 11B). To study reproducibility, the cyclic voltammograms were recorded individually for five electrodes prepared in optimal conditions; the standard deviation of the peak currents was 3.5% (Fig. 11C).

## 4 Conclusion

In this study, the synthesis of an efficient electrochemical sensor to measure MNZ was demonstrated by synthesizing $Co_9S_8@MoS_2$ core–shell nanoparticles and modifying the surface of glassy carbon electrodes with these nanoparticles. The synthesized $Co_9S_8@MoS_2$ core–shell nanoparticles were systematically characterized by SEM, TEM, EDX, XRD, and FT-IR. The electrochemical tests indicated good electrocatalytic activity of the as-prepared sensor toward MNZ. Amperometry was used for the quantification of MNZ, which led to good results in wide linear ranges and at a low LOD. In addition, a $Co_9S_8@MoS_2/$ rGO/GCE sensor was developed for the first time, and the results show that this sensor can detect MNZ in real samples at low concentrations. In addition to being simple and sensitive, this newly developed sensor is low-cost, stable, and offers a large surface area.

**Fig. 11** CVs of the $1 \times 10^{-4}$ M MNZ in 0.1 M of PBS (pH = 7) on the $Co_9S_8@MoS_2$/rGO/GCE sensor with a scanning speed of 50 mV/s, **A** repeated 100 times. **B** with five electrodes. **C** The first, third, fifth, and seventh days
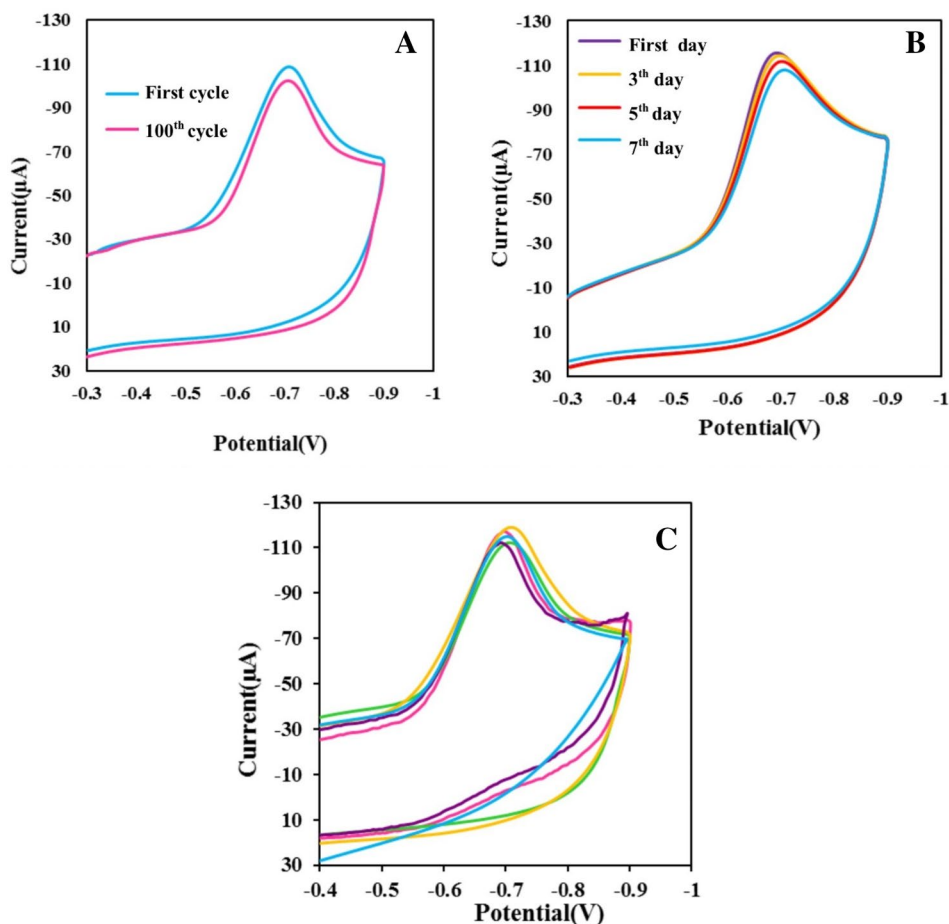
**Data availability** The datasets generated during the current study are available from the corresponding author on reasonable request.

## Declarations

**Conflict of interest** The authors declare that they have no competing financial interests.

## References

1. Rajaji U, Govindasamy M, Sha R, Alshgari RA, Juang RS, Liu TY (2022) Surface engineering of 3D spinel $Zn_3V_2O_8$ wrapped on sulfur doped graphitic nitride composites: investigation on the dual role of electrocatalyst for simultaneous detection of antibiotic drugs in biological fluids. Compos B Eng 242:110017
2. Govindasamy M, Wang SF, Almahri A, Rajaji U (2021) Effects of sonochemical approach and induced contraction of core–shell bismuth sulfide/graphitic carbon nitride as an efficient electrode materials for electrocatalytic detection of antibiotic drug in foodstuffs. Ultrason Sonochem 72:105445
3. Rajaji U, Chen TW, Chinnapaiyan S, Chen SM, Govindasamy M (2020) Two-dimensional binary nanosheets ($Bi_2Te_3$@ g-C3N4): application toward the electrochemical detection of food toxic chemical. Anal Chim Acta 1125:220–230
4. Hasan SH, Abdullah NS (2018) Spectrophotometric methods for determination of metronidazole in pharmaceutical formulations. Zanco J Pure Appl Sci 30(5):89–100
5. Ho C, Sin DW, Wong K, Tang HP (2005) Determination of dimetridazole and metronidazole in poultry and porcine tissues by gas chromatography–electron capture negative ionization mass spectrometry. Anal Chim Acta 530(1):23–31
6. Wang Y, Yao L, Liu X, Cheng J, Liu W, Liu T et al (2019) $CuCo_2O_4$/N-doped CNTs loaded with molecularly imprinted polymer for electrochemical sensor: preparation, characterization and detection of metronidazole. Biosensors Bioelectron 142:111483
7. Kalaiyarasi J, Pandian K (2019) Egg-shell like hollow alumina sphere modified electrode for enhanced electrochemical determination of metronidazole. J Electrochem Soc 166(13):B1151
8. Akay C, Özkan SA, Şentürk Z, Cevheroğlu Ş (2002) Simultaneous determination of metronidazole and miconazole in pharmaceutical dosage forms by RP-HPLC. Il Farmaco 57(11):953–957
9. Gadallah MI, Ali HRH, Askal HF, Saleh GA (2019) Innovative HPTLC-densitometric method for therapeutic monitoring of meropenem and metronidazole in acute pancreatic patients. Microchem J 146:940–947

10. Xia KD, Lu CX, Yang Y (2015) Improving the oxidation resistance of carbon fibers using silicon oxycarbide coatings. New Carbon Mater 30(3):236–243

11. Nagaraja P, Sunitha K, Vasantha R, Yathirajan H (2002) Spectrophotometric determination of metronidazole and tinidazole in pharmaceutical preparations. J Pharm Biomed Anal 28(3–4):527–535

12. Yang G, Zhao F, Zeng B (2014) Magnetic entrapment for fast and sensitive determination of metronidazole with a novel magnet-controlled glassy carbon electrode. Electrochim Acta 135:154–160

13. Kokulnathan T, Chen SM (2019) Praseodymium vanadate-decorated sulfur-doped carbon nitride hybrid nanocomposite: the role of a synergistic electrocatalyst for the detection of metronidazole. ACS Appl Mater Interfaces 11(8):7893–7905

14. Ranganathan P, Mutharani B, Chen SM, Sireesha P (2019) Biocompatible chitosan-pectin polyelectrolyte complex for simultaneous electrochemical determination of metronidazole and metribuzin. Carbohyd Polym 214:317–327

15. Zhu M, Ye H, Lai M, Ye J, Kuang J, Chen Y et al (2018) Differential pulse stripping voltammetric determination of metronidazole with graphene-sodium dodecyl sulfate modified carbon paste electrode. Int J Electrochem Sci 13(4100):73

16. Yuan S, Bo X, Guo L (2019) In-situ insertion of multi-walled carbon nanotubes in the $Fe_3O_4$/N/C composite derived from iron-based metal-organic frameworks as a catalyst for effective sensing acetaminophen and metronidazole. Talanta 193:100–109

17. Yu T, Glennon L, Fenelon O, Breslin CB (2023) Electrodeposition of bismuth at a graphene modified carbon electrode and its application as an easily regenerated sensor for the electrochemical determination of the antimicrobial drug metronidazole. Talanta 251:123758

18. Zokhtareh R, Rahimnejad M, Najafpour-Darzi G, Karimi-Maleh H (2023) A novel sensing platform for electrochemical detection of metronidazole antibiotic based on green-synthesized magnetic $Fe_3O_4$ nanoparticles. Environ Res 216:114643

19. Liu Z, Wang Z, Xu Y (2022) A powerful electrochemical sensor based on $Fe_2O_3$ nanoparticle-graphene oxide nanocomposites for determination of metronidazole as an antibacterial drug. Int J Electrochem Sci 17(220731):2

20. Chinnaraj S, Palani V, Yadav S, Arumugam M, Sivakumar M, Maluventhen V et al (2021) Green synthesis of silver nanoparticle using goniothalamus wightii on graphene oxide nanocomposite for effective voltammetric determination of metronidazole. Sens Bio-Sens Res 32:100425

21. Kesavan G, Chen SM (2021) Sonochemical-assisted synthesis of zinc vanadate microstructure for electrochemical determination of metronidazole. J Mater Sci Mater Electron 32:9377–9391

22. Meenakshi S, Rama R, Pandian K, Gopinath S (2021) Modified electrodes for electrochemical determination of metronidazole in drug formulations and biological samples: An overview. Microchem J 165:106151

23. Baikeli Y, Mamat X, Wumaer M, Muhetaer M, Aisa HA, Hu G (2020) Electrochemical determination of metronidazole using a glassy carbon electrode modified with nanoporous bimetallic carbon derived from a ZnCo-based metal-organic framework. J Electrochem Soc 167(11):116513

24. Xia YM, Ou X, Zhao Y, Xia M, Chen D, Gao WW (2021) Facile synthesis of reduced graphene oxide-octahedral $Mn_3O_4$ nanocomposites as a platform for the electrochemical determination of metronidazole and sulfamonomethoxine. Electroanalysis 33(6):1646–1656

25. Huang J, Qiu Z, Lin J, Lin J, Zhu F, Lai G et al (2023) Ultrasensitive determination of metronidazole using flower-like cobalt anchored on reduced graphene oxide nanocomposite electrochemical sensor. Microchem J 188:108444

26. Mir A, Shabani-Nooshabadi M, Ziaie N (2023) Electrochemical monitoring of metronidazole and oxazepam in plasma sample by using a glassy carbon electrode modified by binary mixed Mof. Available at SSRN 4348580

27. Mariappan K, Alagarsamy S, Chen SM, Sakthinathan S (2023) Electrochemical detection of metronidazole by the fabricated composites of orthorhombic iron tungsten oxide decorated with carbon nanofiber composites electrode. J Electrochem Soc 170(3):037514

28. Mir A, Shabani-Nooshabadi M, Ziaie N (2023) Electrochemical monitoring of metronidazole and oxazepam in plasma sample by using a glassy carbon electrode modified by binary mixed Mof. Available at SSRN 4453403

29. Ponnaiah SK, Prakash P (2020) Carbon dots doped tungstic anhydride on graphene oxide nanopanels: a new picomolar-range creatinine selective enzymeless electrochemical sensor. Mater Sci Eng C 113:111010

30. Vellaichamy B, Ponniah SK, Prakash P (2017) An in-situ synthesis of novel Au@ NG-PPy nanocomposite for enhanced electrocatalytic activity toward selective and sensitive sensing of catechol in natural samples. Sens Actuators B Chem 253:392–399

31. Ponnaiah SK, Periakaruppan P, Selvam M, Muthupandian S, Jeyaprabha B, Selvanathan R (2020) Clinically pertinent manganese oxide/polyoxytyramine/reduced graphene oxide nanocomposite for voltammetric detection of salivary and urinary arsenic. J Clust Sci 31:877–885

32. Vellaichamy B, Periakaruppan P, Ponnaiah SK (2017) A new in-situ synthesized ternary CuNPs-PANI-GO nano composite for selective detection of carcinogenic hydrazine. Sens Actuators B Chem 245:156–165

33. Ponnaiah SK, Prakash P, Vellaichamy B (2018) A new analytical device incorporating a nitrogen doped lanthanum metal oxide with reduced graphene oxide sheets for paracetamol sensing. Ultrason Sonochem 44:196–203

34. Ren H, Gu C, Zhao J, Joo SW, Huang J (2019) $Co_9S_8$@ $MoS_2$ core-shell nanostructure anchored on reduced graphene oxide with improved electrochemical performance for lithium-ion batteries. Appl Surf Sci 473:918–927

35. Hinnemann B, Moses PG, Bonde J, Jørgensen KP, Nielsen JH, Horch S et al (2005) Biomimetic hydrogen evolution: MoS2 nanoparticles as catalyst for hydrogen evolution. J Am Chem Soc 127(15):5308–5309

36. Merki D, Fierro S, Vrubel H, Hu X (2011) Amorphous molybdenum sulfide films as catalysts for electrochemical hydrogen production in water. Chem Sci 2(7):1262–1267

37. Bai J, Meng T, Guo D, Wang S, Mao B, Cao M (2018) $Co_9S_8$@ $MoS_2$ core–shell heterostructures as trifunctional electrocatalysts for overall water splitting and Zn–air batteries. ACS Appl Mater Interfaces 10(2):1678–1689

38. Geng H, Yang J, Dai Z, Zhang Y, Zheng Y, Yu H et al (2017) $Co_9S_8$/$MoS_2$ yolk–shell spheres for advanced Li/Na storage. Small 13(14):1603490

39. Gamfeldt L, Snäll T, Bagchi R, Jonsson M, Gustafsson L, Kjellander P et al (2013) Higher levels of multiple ecosystem services are found in forests with more tree species. Nat Commun 4(1):1–8

40. Choi SH, Kang YC (2015) Synergetic effect of yolk–shell structure and uniform mixing of SnS–MoS2 nanocrystals for improved Na-ion storage capabilities. ACS Appl Mater Interfaces 7(44):24694–24702

41. Chen T, Hu Y, Cheng B, Chen R, Lv H, Ma L et al (2016) Multi-yolk-shell copper oxide@carbon octahedra as high-stability anodes for lithium-ion batteries. Nano Energy 20:305–314

42. Li B, Su Q, Yu L, Zhang J, Du G, Wang D et al (2020) Tuning the band structure of $MoS_2$ via $Co_9S_8@MoS_2$ core–shell structure to boost catalytic activity for lithium–sulfur batteries. ACS Nano 14(12):17285–17294

43. Wu B, Ma R, Liu X, Zheng Y, Guo S, Yi Y et al (2022) Self-assembly synthesis of petal-like $MoS_2/Co_9S_8$/carbon nanohybrids for enhanced lithium storage performance. Front Energy Res 10:1224

44. Liu Y, Geng H, Ang EH, Cao X, Zheng J, Gu H (2019) Hierarchical nanotubes constructed by $Co_9S_8/MoS_2$ ultrathin nanosheets wrapped with reduced graphene oxide for advanced lithium storage. Chem Asian J 14(1):170–176

45. Zhang L, Zhang J, Xu A, Lin Z, Wang Z, Zhong W et al (2023) Charge redistribution of $Co_9S_8/MoS_2$ heterojunction microsphere enhances electrocatalytic hydrogen evolution. Biomimetics 8(1):104

46. Rajaji U, Chinnapaiyan S, Chen SM, Govindasamy M, Alothman AA, Alshgari RA (2021) Bismuth telluride decorated on graphitic carbon nitrides based binary nanosheets: its application in electrochemical determination of salbutamol (feed additive) in meat samples. J Hazard Mater 413:125265

47. Rajaji U, Ganesh PS, Kim SY, Govindasamy M, Alshgari RA, Liu TY (2022) $MoS_2$ sphere/2D $S-Ti_3C_2$ MXene nanocatalysts on laser-induced graphene electrodes for hazardous aristolochic acid and roxarsone electrochemical detection. ACS Appl Nano Mater 5(3):3252–3264

48. Askari MB, Beheshti-Marnani A, Seifi M, Rozati SM, Salarizadeh P (2019) $Fe_3O_4@MoS_2$/RGO as an effective nano-electrocatalyst toward electrochemical hydrogen evolution reaction and methanol oxidation in two settings for fuel cell application. J Colloid Interface Sci 537:186–196

49. Holzwarth U, Gibson N (2011) The Scherrer equation versus the'Debye-Scherrer equation'. Nat Nanotechnol 6(9):534

50. Bharath G, Madhu R, Chen SM, Veeramani V, Mangalaraj D, Ponpandian N (2015) Solvent-free mechanochemical synthesis of graphene oxide and $Fe_3O_4$—reduced graphene oxide nanocomposites for sensitive detection of nitrite. J Mater Chem A 3(30):15529–15539

51. Mahmoudian M, Alias Y, Basirun W, Woi PM, Sookhakian M, Jamali-Sheini F (2015) Synthesis and characterization of $Fe_3O_4$ rose like and spherical/reduced graphene oxide nanosheet composites for lead (II) sensor. Electrochim Acta 169:126–133

52. Khan NA, Ahmad I, Rashid N, Zafar MN, Shehzad FK, Ul-Hamid A et al (2022) Enhanced electrochemical activity of $Co_3O_4/Co_9S_8$ heterostructure catalyst for water splitting. Int J Hydrogen Energy 47(72):30970–30980

53. Tang Y, Chen T, Yu S, Qiao Y, Mu S, Zhang S et al (2015) A highly electronic conductive cobalt nickel sulphide dendrite/quasi-spherical nanocomposite for a supercapacitor electrode with ultrahigh areal specific capacitance. J Power Sources 295:314–322

54. Velusamy V, Palanisamy S, Kokulnathan T, Chen SW, Yang TC, Banks CE et al (2018) Novel electrochemical synthesis of copper oxide nanoparticles decorated graphene-β-cyclodextrin composite for trace-level detection of antibiotic drug metronidazole. J Colloid Interface Sci 530:37–45

55. Sriram B, Baby JN, Wang S-F, Ranjitha MR, Govindasamy M, George M (2020) Eutectic solvent-mediated synthesis of NiFe-LDH/sulfur-doped carbon nitride arrays: investigation of electrocatalytic activity for the dimetridazole sensor in human sustenance. ACS Sustain Chem Eng 8(48):17772–17782